Review

Analysis of Mixing Efficiency in a Stirred Reactor Using Computational Fluid Dynamics †

Adan Ramírez-López [ID]

Department of Industrial Engineering, Technological and Autonomous Institute of México (ITAM),
Rio Hondo #1 col. Progreso Tizapan, México City 01080, Mexico; adan.ramirez@itam.mx
† This work is dedicated to the memory of my friend and colleague Pedro Vite-Martinez.

Abstract: Lead recycling is very important for reducing environmental pollution risks and damages. Liquid lead is recovered from exhaust batteries inside stirred batch reactors; the process requires melting to be cleaned. Nevertheless, it is necessary to establish parameters for evaluating mixing to improve the efficiency of the industrial practices. Computational fluid dynamics (CFD) has become a powerful tool to analyze industrial processes for reducing operating costs, avoiding potential damages, and improving the equipment's performance. Thus, the present work is focused on simulating the fluid hydrodynamics inside a lead-stirred reactor monitoring the distribution of an injected tracer in order to find the best injection point. Then, different injected points are placed on a control plane for evaluation; these are evaluated one by one by monitoring the tracer concentration at a group of points inside the batch. The analyzed reactor is a symmetrical, vertical batch reactor with two geometrical sections: one cylindrical body and a semi-spherical bottom. Here, one impeller with four flat blades in a shaft is used for lead stirring. The tracer concentration on the monitoring points is measured and averaged for evaluating the efficiency inside the tank reactor. Hydrodynamics theory and a comparison between the concentration profiles and distribution of tracer curves are used to demonstrate both methods' similarities. Then, the invariability of the tracer concentration on the monitoring points is adopted as the main parameter to evaluate the mixing, and the best injection point is found as a function of the shortest mixing time. Additionally, the influence of the impeller rotation speed is analyzed as an additional control parameter to improve industrial practices.

Keywords: fluid flow stirring; recycling procedure; evaluation of mixing efficiency; tracer concentration; computational fluid dynamics (CFD)

1. Introduction

Batteries are electrochemical devices used for storing energy generated using a cell packaged with a cathode and an anode submerged in an electrolytic solution [1–12]. Lead and sulfuric acid are in vehicle batteries; these are the most popular product where lead is. Nevertheless, the components are toxic and corrosive, can pollute air, soil, and water, and can also be cause for an explosion or a fire. Moreover, exposure to these components can produce serious health hazards to humans and natural life [1–3,7,13–20]. Zhang, li Sun, and other authors have talked about some industrial methods for recycling hazardous materials. Although lead–acid batteries can be physically recharged many times, their working life is limited, as during each cycle, certain stress is placed on the lead plates, according to the operating conditions [3,4,6,7,9–13]. This causes short circuits and reduces the battery's lifetime [2–5,13]. Prengaman, Hildebrandt, and Tian et al. have been working also on the recycling of lead batteries due to the fact that these are one of the most dangerous wastes in the automotive industry [5–8,12,16–19].

Industrially, lead is collected for recycling and reducing environmental damage. Furthermore, the recycling process uses less energy than refining primary ore [2–8,13,14]. Nowadays, recycling has become a clean economical option for many industrial trials

which want to reduce costs; this fact is a very interesting motivation for studying and improving industrial lead processing [1–4,6–9,14,15]. Furthermore, the evaluation of mixing performance is very important for reducing working times and increasing stirring efficiency. That is the reason why this work can be considered as an initial approach to establish mathematical parameters to evaluate industrial practices and improve the actual procedures [6–8,14,15].

Some authors have been working on the simulation of fluid flows involving lead recycling inside chemical reactors [10–12,19–23]. But the geometrical configuration of reactors and the operating conditions are different for each industrial case, making stirring in chemical reactors a complex problem [5–8,14,15,20–27]. Some of these authors have been working with computer simulations showing concentration profiles as evidence of mixing or making physical models to compare results. Other authors like Debangshu have worked on suspensions of solids in recycling procedures, and Feng Wang has studied the measurement of phase holdups in stirred tanks [9,10,20–27]. But the simulation of stirring inside a tank is a complex problem where many variables are involved in terms of the Navier–Stokes equations, and many phenomena must be solved to understand hydrodynamics. Some authors have been testing this by inducing turbulence effects on solid–liquid suspensions to solve problems related to polymerization [20–23]. Rahimi, Lassin, and others studied hollow impeller effects to validate experimental fluid dynamics using CFD in order to evaluate the influence of the impeller speed [28–30]. Some authors simulated lead bullion in hemispherical vessels known as kettles [9–12,14,15,31–34]. Other authors have studied fluid flow dynamics in reactors for different purposes, such as the analysis of resin beads and ways of scaling up. But hydrodynamic behavior and physical properties are particular for each simulated case [10–12,14,16–19]. These authors have provided important knowledge for understanding the hydrodynamic behavior of fluid in chemical reactors. Other authors have studied the effect of perturbations in stirred tanks [19–25,30,35–38]. Others have been analyzing chemical reactions and the evolution of liquid–liquid phases [17–23,26–29,36–40]. Murthy, Zhong Zhang, Sossa-Echeverria, Szalai, and others have dedicated their works to evidencing the influence of tanks and impeller geometries [16–23,35,36]. Some of them have used the residence time distribution method to analyze efficiency in a stirred tank [12,15,26–34,41–43]. Others have simulated dissolutions in tanks and validated these procedures as appropriate for establishing physical parameters to improve mixing [11,12,16–29]. In 2016, Divyamaan worked on a computer simulation of solid–liquid stirred tanks. Tamburini et al. have produced similar works considering solid–liquid suspension and predicting the solid particle distribution and the minimum impeller speed for homogeneous mixing. To conclude, an understanding of the hydrodynamics phenomena involved is very important to improve actual industrial practices in many metallurgical processes [17–30,35,36,39–42,44–49]. Some authors have been studying problems of phenomena related to fluids confined in industrial tanks such as the solid suspension of particles involving chemical reactions evaluating fluid hydrodynamics behaviors under symmetrical and asymmetrical jet conditions [32–34,36–40,43–45,50–52]. Authors have also been developing numerical methods and new approaching techniques for fluid evaluation [6–8,14,15,31–34,42,43,50], inclusively, other metallurgical problems where pyro-processing and the hydrodynamics of liquid metals can be analyzed to improve industrial practices [11,12,16–18,26–29,31–34,41–43].

2. Geometrical Model (Tank Reactor and Impeller)

As was commented previously, there are many aspects influencing the mixing process in chemical batch reactors: the geometry of the batch, impeller mechanisms, industrial working conditions, and properties of the fluids and phases. Moreover, the considerations that are selected, like the use of laminar conditions or the inclusion of mathematical turbulence models, can affect results. Then, in the present work, the geometrical configuration of the reactor was built computationally based on real industrial data. A simulation of the hydrodynamics fluid flow is performed using the software Fluent (6.0), and the re-

sults of the tracer concentration on each monitoring node are saved at every time step ($t + \Delta t$) on independent files to be analyzed using Microsoft Excel in order to evaluate the mixing efficiency [9,10,14,15,25–29]. These values are compared with tracer concentration profiles in order to find zones with good or poor mixing and its contribution to the entire homogeneity.

The industrial reactor analyzed consists of two parts. The first is the main upper body with a cylindrical form and the second is a semispherical section on the bottom, as shown in Figure 1. The cylindrical diameter is 0.44 m, and the cylinder is 0.470 m high. The reactor is symmetrical along the vertical and horizontal axes. Then, a triangular mesh using two-dimensional elements which form a surface model is defined for the walls discretization, since it is only necessary to declare the surface of the reactor walls as a closed boundary [7–11,14,15,25,41,42,48,49]. These walls are also declared free of defects and friction. The mesh used for discretization is not structured with 1062 cells and a regular size. The two sections were traced assuming the center on the cylindrical section at the lowest position and the top center of the semispherical bottom. This intersection point is taken for reference as the origin for the tank (0, 0, 0). Then, we defined two original planes which were joined forming only one single surface that cuts the batch reactor symmetrically.
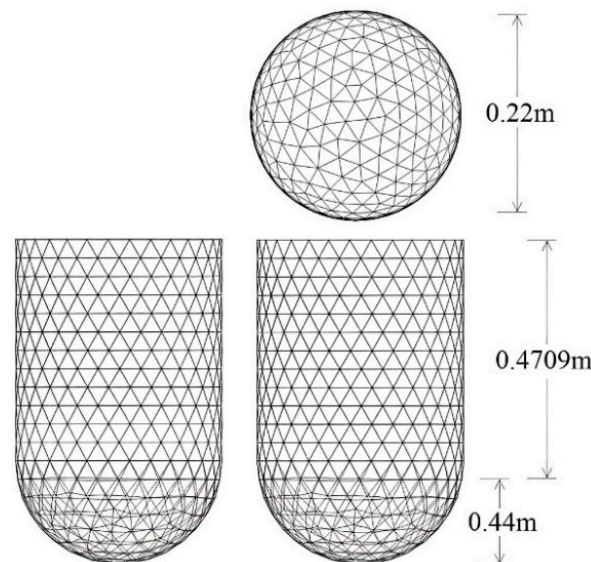

Figure 1. Geometrical model of the tank reactor; two-dimensional views (side left, frontal and upper).

The areas measured of the cylindrical and semispherical sections are 0.66922116 m^2 and 0.282244 m^2, respectively, forming a solid wall with 0.9514656 m^2. A non-structured mesh with triangular cells was selected for a good fit with the cylindrical and semispherical regions of the reactor.

The industrial reactor was stirred using one single impeller formed with a vertical shaft and two rectangular flat solid blades joined in the low shaft position, as can be appreciated in Figure 2a,b. The shaft is 0.610 m in length: enough to be placed inside the reactor, and the four rectangular blades (0.0508 m × 0.0254 m) are form from the intersection of the two flat solids. These blades are placed symmetrically (each 90°) and are 0.00375 m thick. Here, a mesh with triangular 2D and tetragonal 3D cells is used again for the discretization of the entire element surface. The shaft is discretized using 16,890 two-dimensional cells, 657 two-dimensional cells are used for each impeller blade, and the measured area for the shaft is 0.1476181 m^2.
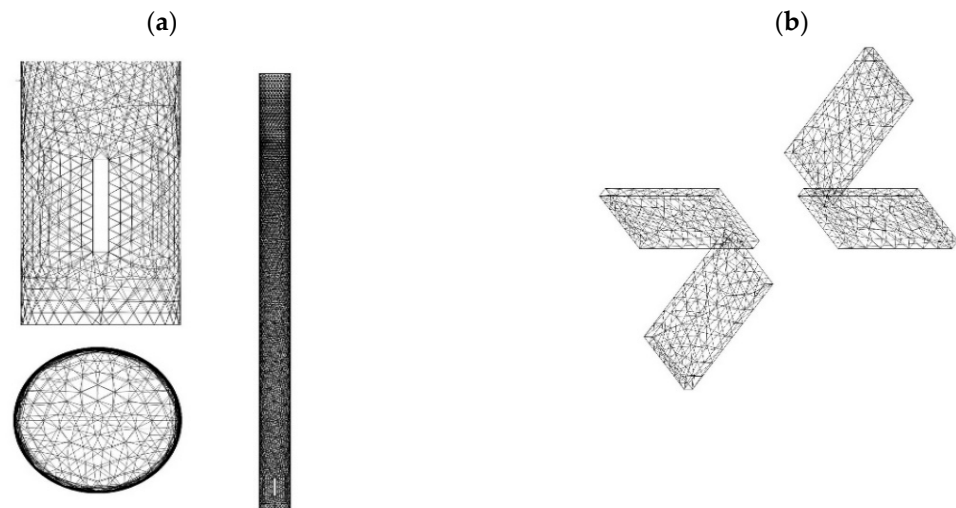
Figure 2. Geometrical model impeller: (**a**) shaft mesh, (**b**) views of the four blades meshed.

The lead bulk volume inside the reactor is obtained applying an inverse negative geometrical Boolean operation. The volume results from the original volume between the walls minus the impeller volume, which was discretized using 22,097 nodes forming 210,235 two-dimensional cells (triangular), which forms 99,923 tri-dimensional cells (tetrahedral). To obtain a good approach, the smallest cell elements were placed near the impeller, and the biggest cells were placed near the wall reactor, since the contact with the impeller for the fluid movement simulation is very important. Moreover, the volume of the tank obtained is the volume of liquid lead simulated.

Additionally, the tank reactor was modeled using different types of meshes, as is shown in the validation section and also was compared with a basic physical model.

3. Semi-Planes, Injection and Monitoring Points, and Initial Assumptions

The reactor is symmetrical vertically; here, a control plane is taken for reference purposes, as shown in Figures 3 and 4. The control plane was divided into two semi-planes. The first of them was the injection plane. Here, all the nodes where the tracer would be injected for each simulation were indicated. All of these were evaluated independently in order to find the best injection point. The second plane was the monitoring plane. Here, we placed the points where the mixing efficiency would be measured and evaluated. The position of every point of both planes is shown in Tables 1 and 2, respectively.

Table 1. Position of the injection points on the semi-plane (coordinates).

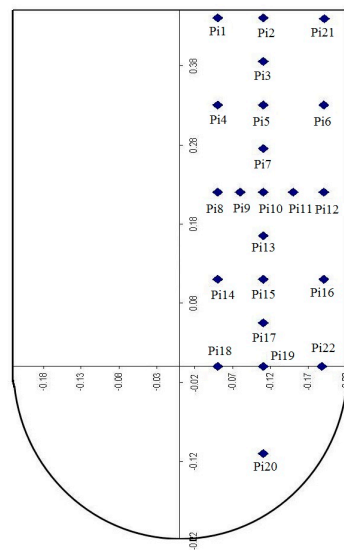| Position (m)	Pi$_1$	Pi$_2$	Pi$_3$	Pi$_4$	Pi$_5$	Points Pi$_6$	Pi$_7$	Pi$_8$	Pi$_9$	Pi$_{10}$	Pi$_{11}$
x	0.050	0.110	0.110	0.050	0.110	0.190	0.110	0.050	0.080	0.110	0.150
y	0.440	0.440	0.385	0.330	0.330	0.330	0.275	0.220	0.022	0.220	0.220
	Pi$_{12}$	Pi$_{13}$	Pi$_{14}$	Pi$_{15}$	Pi$_{16}$	Pi$_{17}$	Pi$_{18}$	Pi$_{19}$	Pi$_{20}$	Pi$_{21}$	Pi$_{22}$
x	0.190	0.110	0.050	0.110	0.190	0.110	0.050	0.110	0.110	0.190	0.190
y	0.220	0.165	0.110	0.110	0.110	0.055	0.000	0.000	−0.110	0.440	0.000

Figure 3. Control semi-plane showing the position of every analyzed injection point (points placed to the right of the central line of the batch reactor).
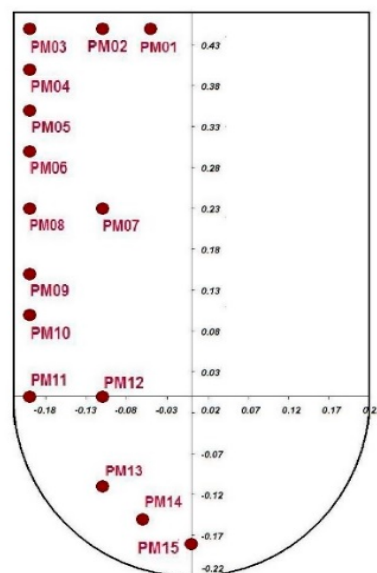

Figure 4. Control semi-plane showing the monitoring points (points placed to the right of the central line of the batch reactor).

Table 2. Position of the monitoring points on the semi-plane (coordinates).

Position (m)	Points							
	Pm_1	Pm_2	Pm_3	Pm_4	Pm_5	Pm_6	Pm_7	Pm_8
x	−0.200	−0.200	−0.200	−0.200	−0.200	−0.200	−0.200	−0.200
y	0.450	0.400	0.350	0.300	0.230	0.150	0.100	0.000
	Pm_9	Pm_{10}	Pm_{11}	Pm_{12}	Pm_{13}	Pm_{14}	Pm_{15}	
x	−0.110	−0.110	−0.110	−0.110	−0.060	−0.050	0.000	
y	0.450	0.230	0.000	−0.110	−0.150	−0.165	−0.180	

The injection points were placed on different places to know their position influence on the injection semi-plane and evaluate the changes on the hydrodynamic behavior with a common reactor geometry and impeller during specific rotatory conditions, enabling identifying death zones (zones with poor mixing) and zones with delays in mixing. The

points (Pi_1, Pi_4, Pi_8, Pi_{14}, and Pi_{18}) are placed along the shaft from the reactor surface to the blades. The nearest injection points to the wall are Pi_6, Pi_{12}, Pi_{16}, Pi_{21}, and Pi_{22}. The points in the middle tank position are Pi_2, Pi_3, Pi_5, Pi_7, Pi_{10}, Pi_{13}, Pi_{15}, and Pi_{17}. Finally, only one single point was placed on the bottom for evaluating hydrodynamic behavior in this zone (Pi_{20}). Here, the sub-index "i" is used to indicate the injection point.

The parameter to evaluate mixing efficiency inside the entire reactor is the tracer distribution. This was conducted by measuring it on each monitoring point. The monitoring points were also placed all around the semi-plane to measure the tracer concentration in different zones inside the tank. The purpose is to identify zones with rich and poor mixing and relate them with the hydrodynamic behavior and the evolution of tracer dispersion. The monitoring points were placed on the monitoring semi-plane at 180° from the injection semi-plane, as shown in Figure 4. These points were used for saving the tracer concentration (C_m) at every time step ($t + \Delta t$) during the simulation. Here, the sub-index "m" is used to indicate the monitoring points. Initially, for $t = 0$, it is assumed the tracer concentration on each monitoring point is equal to zero ($C_m = 0$). Some of these points were placed in the middle of the reactor such as Pm_2, Pm_7 and Pm_{12}; some others were placed near the walls such as Pm_{03} to Pm_{06} and Pm_{08} to Pm_{11}. Finally, the rest of these were placed at the bottom such as Pm_{13}, Pm_{14} and Pm_{15}. Here, evaluation is very important because this region is critical for mixing.

4. Assumptions

The following assumptions and boundary conditions are taken into account for all the simulations exposed in this work:

- The impeller shaft is in the middle position of the reactor body for symmetrical conditions. Additionally, no vibration is assumed during rotation; then, the influence of the shaft rotation is not significant. Consequently, the only elements that provide stirring to the bath are the four blades.
- Rugosity on tank walls (cylinder and semispherical) is neglected as a consequence of the fluid displacement being free, and no drag is induced.
- The impeller rotates at 200 radians per minute: approximately 32 RPMs.
- The surface of the liquid lead is flat; this condition is equivalent to assuming a closed reactor on the tank top. The lead surface is discretized with 1512 two-dimensional cells, and the measured area is 0.149812 m^2.
- The maximum face area for a cell used for discretization is 1.9733×10^{-3} m^2 in contrast the minimum cell face area is 2.0324×10^{-6} m^2.
- The temperature of liquid lead is assumed as 327.46 °C (equal to 600.61 K or 621.43 F). This is the lead melting point, and the lead density equal to 10.66 g/cm^3. Then, liquid lead is a heavy incompressible fluid.
- During all analyzed cases on simulations, no heat interchange is assumed (isothermal system); then, the lead properties remain constant.
- The tank is considered as isolated, there is no mass interchange, the volume is constant inside, and the tracer replaces a defined lead volume in the 3D mesh.
- The movement of fluid is not a step pulse defined and not a continuous injection; the tracer volume replaced is moved as a consequence of the inertial forces due to the impeller impulse.
- The time step (Δt) used for simulation was 5.208×10^{-3} and represents a rotation of 1° around the tank circumference considering the rotatory speed of the impeller.
- There is no volume or mass interchange during the simulation; moreover, the movement of the fluid is due exclusively to the inertial forces of the velocity generated by the impeller movement.

The tracer takes place (is injected computationally) inside the tank reactor when the velocity of the fluid is stable. Then, this is considered as the beginning of the simulation cases. The distribution of the velocity vectors due to the impeller rotation can be appreciated in Figure 5a–c; here, the biggest vectors can be appreciated near the blades, and the smallest

vectors are in the tank body. During experimental mixing operations, a tracer can be injected using a tubing inlet system submerged into the bath. Nevertheless, this is not performed in the present work. The tracer cannot be injected computationally. The simulation is performed by replacing a defined lead volume, which is 125 cm^3 = 1.25×10^{-4} m^3. Then, the tracer distribution is saved and evaluated dynamically as simulations run. During every simulation, only one single lead volume is replaced on the injection cells by an identical tracer volume at the beginning of the simulation ($t = 0$). Consequently, the tracer is assumed as ideal; then, an original lead volume is substituted by another volume with the same physical properties. This method is frequently used by authors who work on physical and computer simulation to evaluate fluid flows [1–5,10–13,16–18,30,35–40]. This procedure is conducted experimentally using colorants for painting the original fluid in order to follow the fluid path and show streamlines of fluid [5–7,13,26–30,39,40,44–46]. Nevertheless, in real industrial practices, solid chemicals for cleaning lead are incorporated to the bath tank using a lance inside. The lance can be placed at different positions in the cylindrical body; but, geometrically, it is complicated to inject below the impeller.
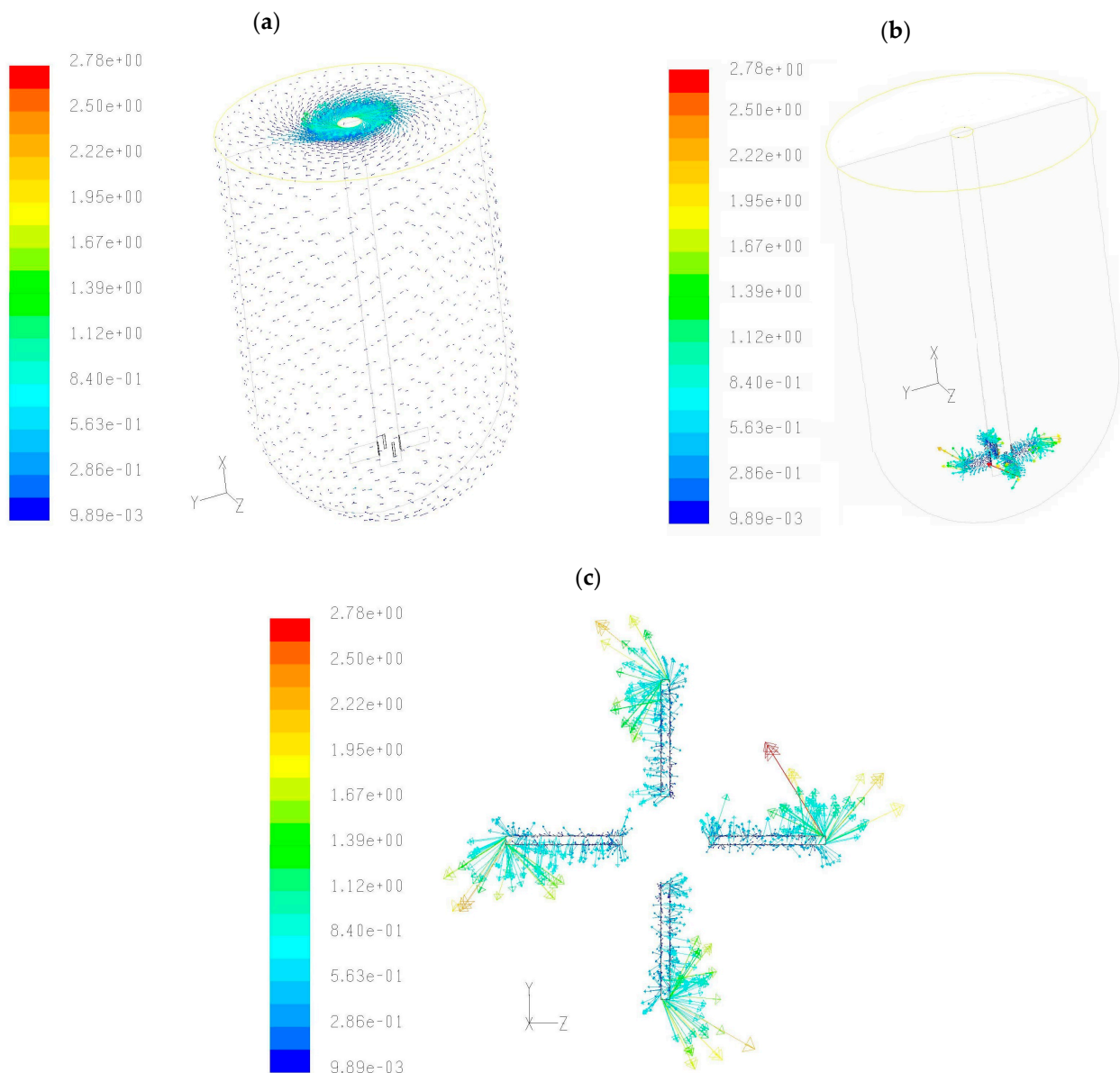
(**a**)

(**b**)

(**c**)

Figure 5. Velocity vector distribution (**a**) all around the entire tank and (**b**,**c**) on the blades of the impeller.

5. Mathematical Modeling

The equations solved on the mathematical model are given by Navier–Stokes and continuity. The Navier–Stokes equations describe the motion of fluids. These equations arise from applying Newton's second law [10–12,16–18,24–30,35,36]. The Navier–Stokes equations are nonlinear partial differential equations in almost every real situation. In some cases, such as one-dimensional flow, these equations can be simplified to linear equations. Nevertheless, nonlinearity carries most problems that are difficult or impossible to solve with conventional analysis because the main contributor is turbulence [9–12,16,26–30,35–38]. The numerical solution of the Navier–Stokes equations for turbulent flows is complex due to the significantly different mixing length involved in turbulent flow. Then, the stable solution of these equations requires the definition of a fine mesh during discretization to make the computational treatment of data feasible [5,23–29,36–39]. Turbulence models such as the k-ε model are used in practical computational fluid dynamics (CFD) applications where turbulent flows are modeled as is shown in this work [32–39]. The Navier–Stokes equations are strictly a statement of the conservation of momentum laws. Thus, in order to describe fluid flow, more information is required according to particular geometrical case data and including particular boundary conditions. Moreover, the basic concepts involved are the conservation of mass and the conservation of energy related to an equation of state [30,35–38,45–48]. All these must be appropriately established. Then, a statement of the conservation of mass is achieved through the mass continuity equation, as shown in Equation (1).

$$\frac{\partial p}{\partial t} + \nabla \times (\rho v) = 0 \tag{1}$$

Then, Navier–Stokes equations can be solved in three coordinate systems; here, Cartesian is the system solved and equations are taken directly from the vector equations [36–40]. The solution implies the programming of Equations (2)–(4) using an explicit numerical method. Here, the velocity components are typically named u, v, and w, which are the dependent variables to be solved.

$$\rho\left(\frac{\partial u}{\partial t} + u\frac{\partial u}{\partial x} + v\frac{\partial u}{\partial y} + w\frac{\partial u}{\partial z}\right) = -\frac{\partial p}{\partial x} + \mu\left(\frac{\partial^2 u}{\partial x^2} + \frac{\partial^2 u}{\partial y^2} + \frac{\partial^2 u}{\partial z^2}\right) + \rho g_x \tag{2}$$

$$\rho\left(\frac{\partial v}{\partial t} + u\frac{\partial v}{\partial x} + v\frac{\partial v}{\partial y} + w\frac{\partial v}{\partial z}\right) = -\frac{\partial p}{\partial y} + \mu\left(\frac{\partial^2 v}{\partial x^2} + \frac{\partial^2 v}{\partial y^2} + \frac{\partial^2 v}{\partial z^2}\right) + \rho g_y \tag{3}$$

$$\rho\left(\frac{\partial w}{\partial t} + u\frac{\partial w}{\partial x} + v\frac{\partial w}{\partial y} + w\frac{\partial w}{\partial z}\right) = -\frac{\partial p}{\partial z} + \mu\left(\frac{\partial^2 w}{\partial x^2} + \frac{\partial^2 w}{\partial y^2} + \frac{\partial^2 w}{\partial z^2}\right) + \rho g_z \tag{4}$$

Note that gravity was assumed as a body force, and the values of g_x, g_y, and g_z will depend on the orientation of gravity with respect to the chosen set of coordinates; for the reactor analyzed, g_x and g_y will be equal to zero; and only g_z participates in the fluid motion. Then, the continuity equation can be written as follows:

$$\frac{\partial p}{\partial t} + \frac{\partial(\rho u)}{\partial x} + \frac{\partial(\rho v)}{\partial y} + \frac{\partial(\rho w)}{\partial z} = 0 \tag{5}$$

When the flow is at a steady state, (ρ) does not change with respect to time. Instead, the continuity equation can be simplified to:

$$\frac{\partial(\rho u)}{\partial x} + \frac{\partial(\rho v)}{\partial y} + \frac{\partial(\rho w)}{\partial z} = 0 \tag{6}$$

When the flow is incompressible, ρ is constant and does not change with respect to space or time, and the continuity equation is reduced again to:

$$\frac{\partial u}{\partial x} + \frac{\partial v}{\partial y} + \frac{\partial w}{\partial z} = 0 \tag{7}$$

The partial differential equation for the mass transfer (equation of continuity) can be written in rectangular coordinates as is shown in Equation (8) and in cylindrical and spherical coordinates as shown in Equations (9) and (10), respectively, representing a solution for the Fick's law equation; these equations can be solved for regular structured or non-structures and hexahedral or tetragonal or any other cells incorporated in nested loops and using a finite element method. Here, the k-ε model is used to solve the problem including turbulence; then, tracer concentration values over monitoring points are stored after every time step ($p_m{}^{t+\Delta t}$); finally, data are analyzed using Microsoft Excel. It is important to mention that the tank with a mix of lead + tracer can be considered as a multicomponent fluid problem, as represented in Equation (11) [42]. Here, D_{eff} is the diffusion and turbulent coefficient.

$$\frac{\partial c_A}{\partial t} = D_{AB}\left[\frac{\partial^2 c_A}{\partial x^2} + \frac{\partial^2 c_A}{\partial y^2} + \frac{\partial^2 c_A}{\partial z^2}\right] \tag{8}$$

$$\frac{\partial c_A}{\partial t} = D_{AB}\left[\frac{\partial^2 c_A}{\partial r^2} + \frac{1}{r}\frac{\partial c_A}{\partial r} + \frac{1}{r^2}\frac{\partial^2 c_A}{\partial \theta^2} + \frac{\partial^2 c_A}{\partial z^2}\right] \tag{9}$$

$$\frac{\partial c_A}{\partial t} = D_{AB}\left[\frac{1}{r^2}\frac{\partial}{\partial r}\left(\frac{\partial c_A}{\partial r}\right) + \frac{1}{r^2 \sin\theta}\frac{\partial}{\partial \theta}\sin\theta\frac{\partial c_A}{\partial \theta} + \frac{1}{r^2 \sin^2\theta}\frac{\partial^2 c_A}{\partial \phi^2}\right] \tag{10}$$

$$\frac{\partial}{\partial t}(\rho_l C) + \nabla \times (\rho_l u_l C) = \nabla \times (\rho_l D_{eff} \nabla C) \tag{11}$$

6. Computer Simulations

The model used for simulation was (k-ε), and the software used for solving was Fluent 6.0; hydrodynamic behavior is studied calculating and saving the tracer concentration at each step ($t + \Delta t$) during simulations on every monitoring point. Figure 6a–c show the tracer concentration on all the monitoring points for the injection points Pi_{11}, Pi_{18}, and Pi_{21}, respectively. These monitoring points were placed inside the tank, near and far from the impeller. Some of the curves in these figures show parabolic behavior and others are sinusoidal. Sinusoidal curves are near the impeller; here, the tracer concentration changed at every time step during simulation due to the strong influence of turbulence and vector velocities. In contrast, parabolic behavior is frequently observed near the walls and at the bottom of the tank, where the homogenization of tracer concentration is very slow, and no strong fluctuations are presented because these points are far away from the impeller influence. The tracer begins to be distributed by stirring from values equal to zero (the tracer is absent on monitoring points). Then, as the simulation time advances, there are some periods when the tracer concentration is increased and others when it is decreased. Nevertheless, these fluctuations are reduced as the simulation continues. The reduction on this fluctuation is considered as a parameter to evaluate mixing. Thus, for long times, all the monitoring points tend to adopt the same averaged concentration. This means that the tracer has been homogeneously distributed. There are curves with high tracer saturations on Figure 6a,c; this is not good for mixing; these excesses must be stirred to obtain a homogeneous distribution. Figure 6a shows that only a few curves are parabolic and remain always with a low tracer concentration. Nevertheless, these curves take a lot of time to reach the final average concentration, indicating poor mixing in these regions. Thus, according to the time scales in the horizontal axes, it is possible to appreciate that the best injection point is Pi_{18}; here, the tank delay is only 450 s. On the other hand, the worst

injection point is Pi_{21} with delays of more than 1400 s, and the tracer distribution injecting on Pi_{11} is considered as an intermediate behavior.
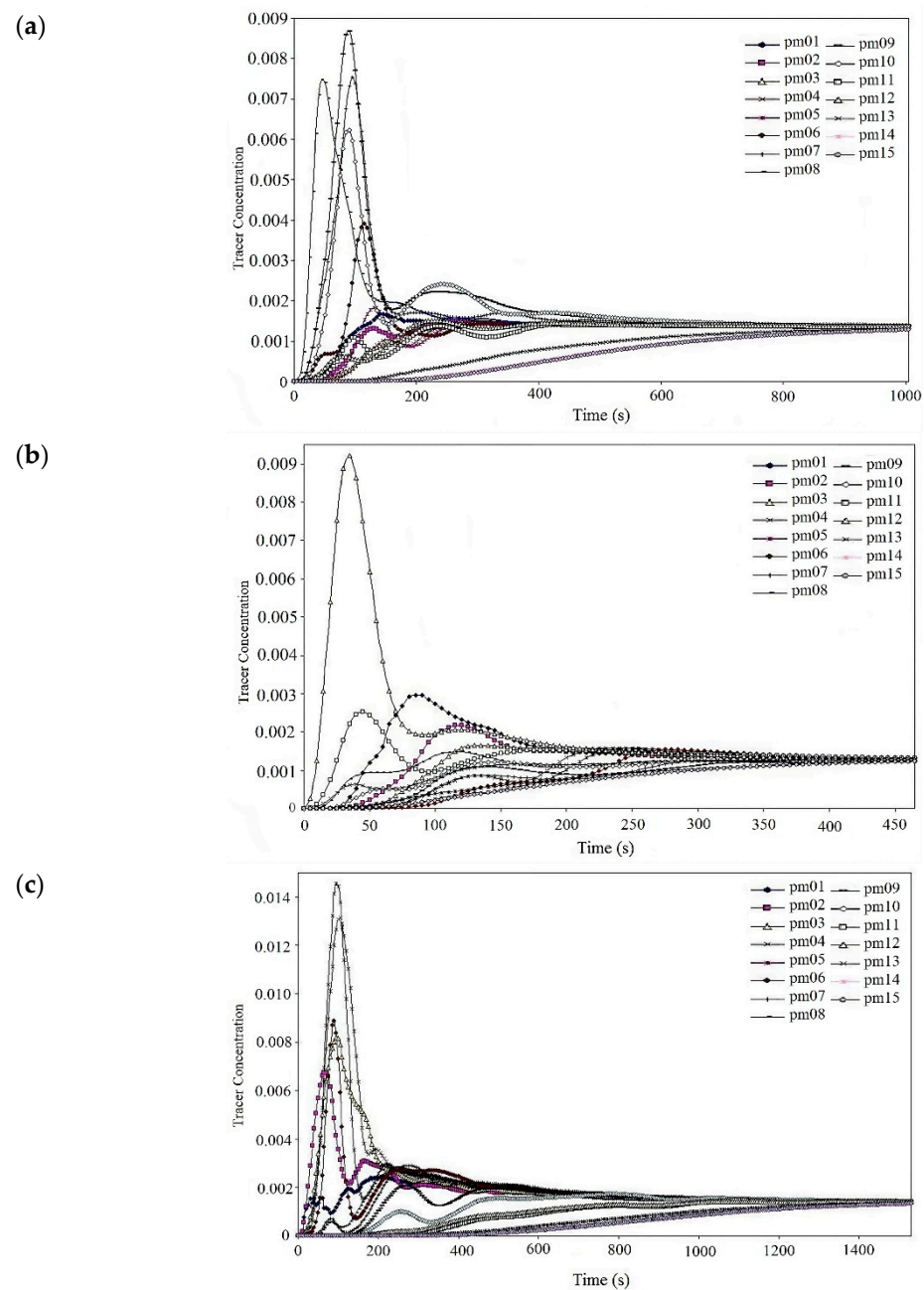

Figure 6. Tracer concentration curves for all the monitoring points (**a**) corresponding to the injected point (Pi_{11}); (**b**) corresponding to the injected point (Pi_{18}); and (**c**) corresponding to the injected point (Pi_{21}).

In Figure 6b, only one curve presents a high tracer concentration, and others have minor excesses. This means that minor stirring work must be applied for mixing. Figure 6c shows there are some curves with high tracer concentrations, but there are also many curves with a very poor concentration which are located near the bottom, because accessing this zone is very difficult. Moreover, all curves tend to the same the final value; this variability is considered as homogeneity criterion for the mixing. Thus, finding the best injection point is the first way to improve industrial practices. In Figure 6a–c, similar behavior can be appreciated on the corresponded monitoring points for every different injection point; nevertheless, curves are affected by the analyzed injection point.

Tracer concentration on all the monitoring points can be stored and then averaged to obtain a significant value of the tracer concentration inside the reactor which represents the entire behavior. Equation (12) can be used to represent this process; here, the sum in the numerator is the contribution of every monitoring point where tracer concentration was measured, and 15 is the number of monitoring points. Then, this is repeated during every time step ($t + \Delta t$) for every corresponding injection point (C_I). Figure 7 shows these averaged curves to illustrate the general tracer concentration for the best, an intermediate and the worst injection points. Here, it is possible to confirm Pi_{18} is the best injection point. The curve is lightly sinusoidal, but fluctuations are quickly damped; thus, the curve tends to the final tracer concentration value and no more than 450 s is required for the mixing. This curve is just above the final tracer concentration, and the fluctuations are minors and quickly damped. In contrast, the worst injection point is Pi_{21}, where there is too much of a time delay because many of the curves are parabolic and distribution is very slow.

$$C_i^{t+\Delta t} = \frac{\sum\limits_{mp=1}^{mp=15} C_{mp}^{t+\Delta t}}{15} \tag{12}$$
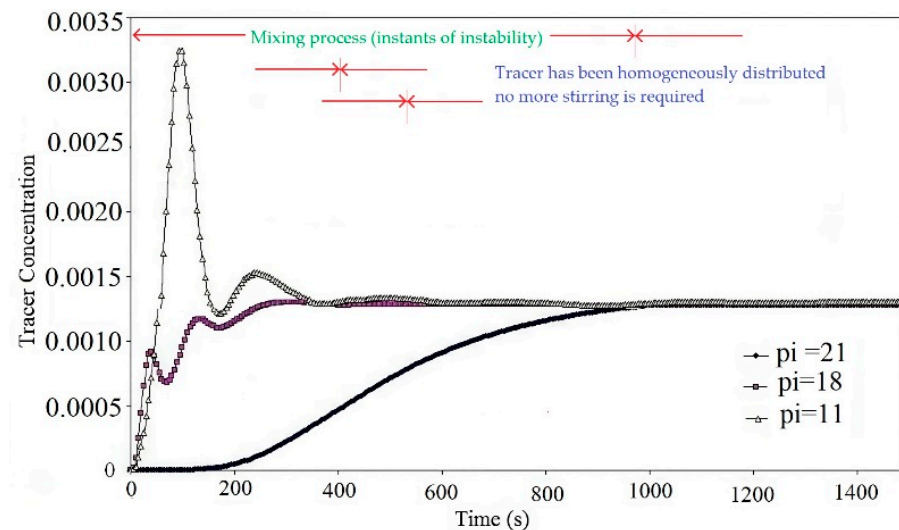

Figure 7. Tracer concentration for the best, intermediate, and worst injection points (Pi_{18}, Pi_{11}, Pi_{21}, respectively); curves for averaged behavior.

The injection point Pi_{11} shows a moderate behavior, because it was placed between the shaft and the wall (in a middle distance). Its curve is also sinusoidal, although a high excess of tracer concentration is appreciated at short simulation times. This variation is also quickly stabilized as time passes, but the time required for a good mixing is near 600 s. Moreover, the fluctuations are so high in comparison with those for the injection point Pi_{18}. This curve is initially significantly above the final tracer concentration value. Then, this instability must be reduced applying additional stirring in comparison with the point Pi_{18}.

Pi_{21} is the worst injection point. Here, the hydrodynamic behavior is very different. Mixing is delayed due to the tracer being slowly distributed. The time required for mixing considering this injected point is more than 900 s. This curve is always below the final tracer concentration value due to the difficulty for the distribution all around the tank. This injection point is placed near the top corner of the cylindrical section of the tank; it is very far from the impeller influence. Then, the evolution of tracer distribution is very slow. Furthermore, the buoyancy of tracer is critical for the simulation on the semispherical region because it is so difficult to distribute tracers in this region. Moreover, in Figure 7, it can be seen that the final tracer concentration all around the tank for all the injected points tends to a final value which is considered as the moment when the tracer has been

homogeneously distributed and no additional stirring is required. Consequently, the best injection point is with the shortest mixing time as indicated.

Figure 8a–d show the tracer concentration profiles on the reactor for the best injection point (Pi$_{18}$). Here, colors indicate regions where the tracer has or has not been distributed. Figure 8a was snapped at the initial time ($t = 0$). Here, the tracer is originally injected. Figure 8b was snapped at 250 s. There are regions with an excess of tracer concentration, but there are some other regions with a poor tracer concentration such as those near the bottom and the highest corner on the cylinder. Figure 8c was taken at 500 s, and it shows a distribution that is nearly homogeneous. There are four zones remaining with lower different tracer concentrations, which are near the cylinder top region, although the profile shows a very similar tracer concentration generally. Figure 8d shows a profile with the same color in the entire reactor. It means that the all the liquid lead and the tracer are perfectly mixed due to stability and homogeneity criterions. Moreover, for all these figures, the color scales are reduced as the mix inside the tank tends to be homogeneous.
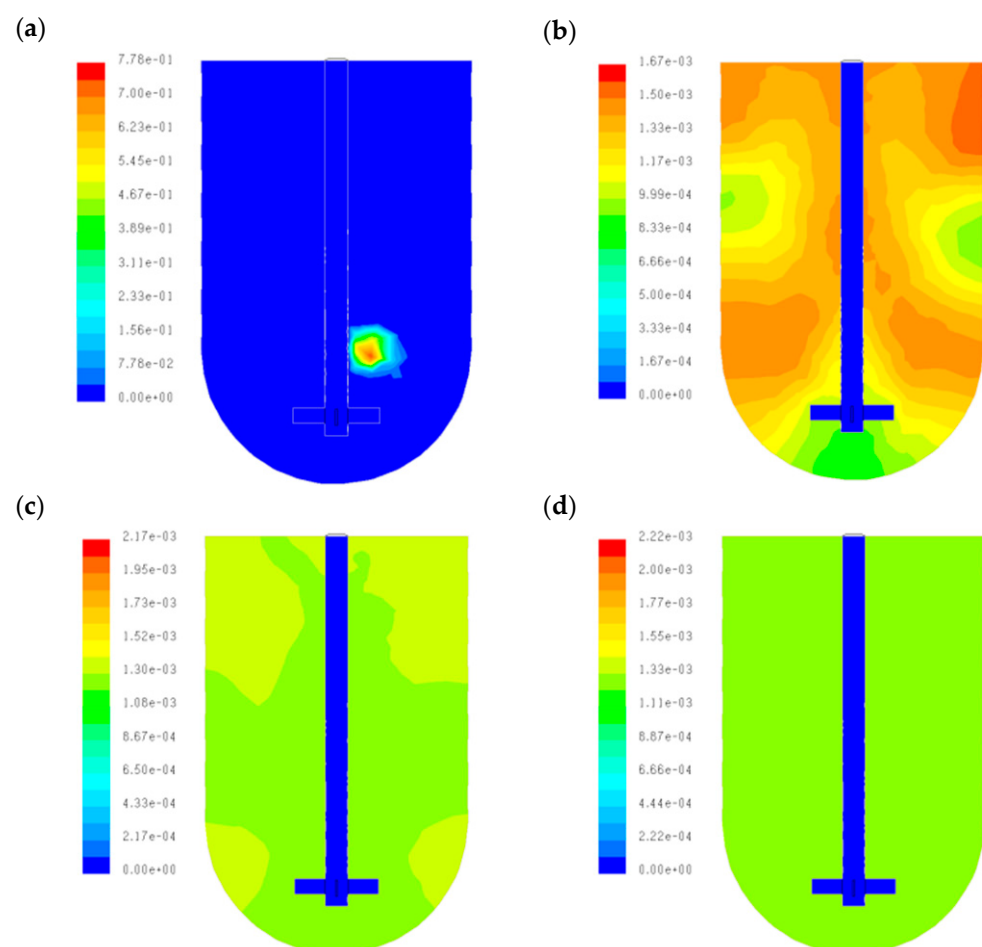

Figure 8. Tracer concentration profiles at different simulation times for the injection point (Pi$_{18}$). (**a**) $t = 0$ s, (**b**) $t = 250$ s, (**c**) $t = 500$ s (**d**) $t = 750$ s.

Figure 9a–d show the tracer concentration on the reactor for a point assumed to have intermediate behavior (Pi$_{11}$). Figure 9a was also taken at time t = 0; again, it is possible to identify where the injection point is placed. In Figure 9b, the tracer has begun to be distributed on the reactor, but there are regions with a high and a low tracer concentration in the cylindrical section. Nevertheless, big zones with a low tracer concentration are in the reactor bottom. In Figure 9c, high tracer concentrations remain on the cylindrical section near the tank walls. The tracer has been introduced in the reactor bottom, but the profile is still not homogeneous. Finally, Figure 9d shows the progress of the tracer

distribution all around the reactor; zones with very high and low tracer concentrations have disappeared, and the profile is certainly more homogeneous. However, this distribution has a low efficiency in contrast with that shown in Figure 8a–d, and longer times for stirring are necessary for a good mixing.
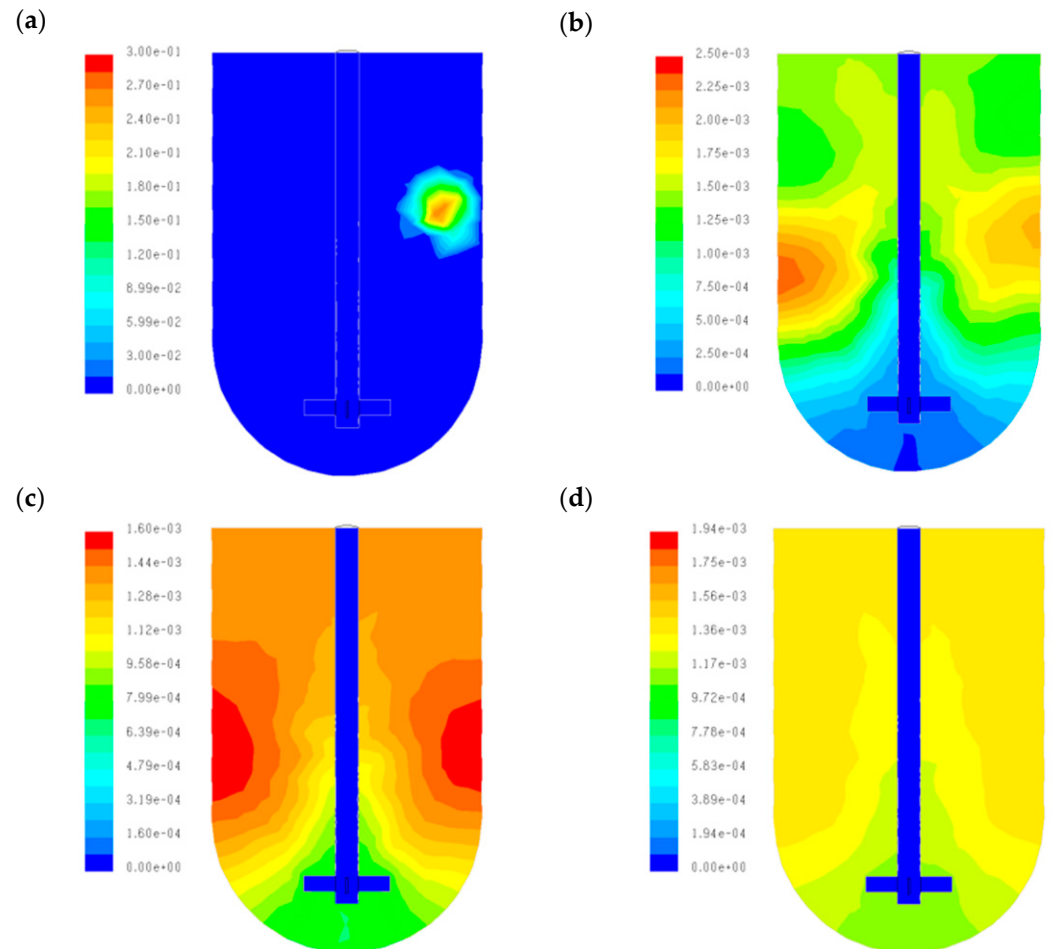

Figure 9. Tracer concentration profiles at different simulation times for the injection point (Pi_{11}). (**a**) $t = 0$ s, (**b**) $t = 250$ s, (**c**) $t = 500$ s, (**d**) $t = 750$ s.

Figure 10a–d show the tracer concentration for the worst injection point (Pi_{21}). Here, the tracer is injected into a point near the reactor top surface and the wall; this is a very isolated region and velocity vectors are weak here, as is shown in Figure 10a. This point is placed far away from the impeller, and the influence of the rotational movement is weak. As a consequence, the tracer distribution is very slow, as shown in Figure 10b–d. Here, the tracer begins to appear in regions of the cylindrical section, but the bottom of the tanks remains without tracer presence. Nevertheless, huge regions without tracer presence can be appreciated in the middle low cylindrical region and the reactor bottom due to the slow diffusion. The final profile on Figure 10d shows a heterogeneous tracer distribution, indicating the mixing efficiency is very poor, as the tracer has not been distributed in the entire reactor. Moreover, Figures 8–10 show that the most difficult zone is the semispherical zone. This behavior can be confirmed observing the curves in Figures 6 and 7 for the bottom region.
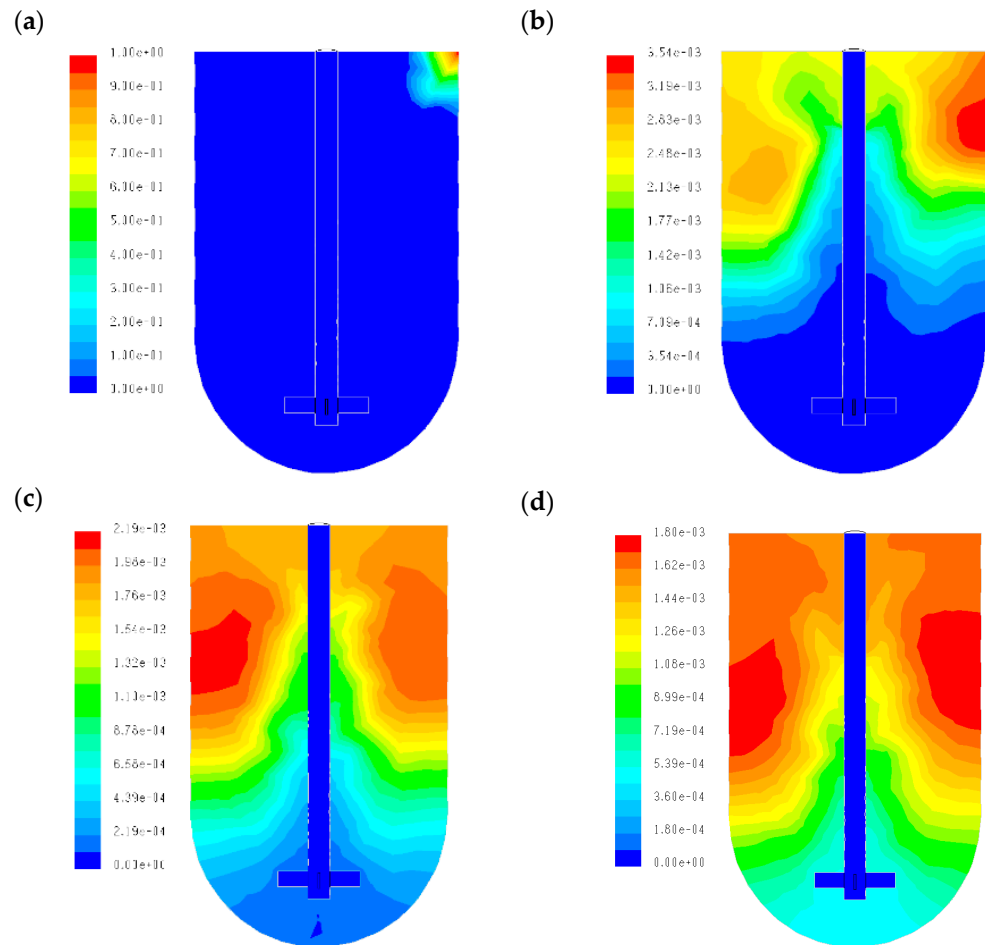
(**a**)

(**b**)

(**c**)

(**d**)

Figure 10. Tracer concentration profiles at different simulation times for the injection point (Pi_{21}). (**a**) $t = 0$ s, (**b**) $t = 250$ s, (**c**) $t = 500$ s, (**d**) $t = 750$ s.

Furthermore, Figures 8–10 show the following:

- The inertial force induced by the impeller begins to break the stationary condition of the liquid lead inside the tank.
- The distribution of tracer inside any tank reactor involves the effect of the fluid displacement, which depends on the forces applied by the impeller movement.
- The tracer initially placed near the impeller is quickly distributed in comparison with the tracer placed near the top or the tank walls.
- The fluid is re-driven as a function of the tank geometry; thus, the hydrodynamics is different when the fluid makes contact with the cylindrical wall than when it takes the flat top or the semispherical bottom.
- The tracer concentration distribution is different on each monitoring point at every time step according with its position on the tank and the injection point analyzed.
- The final tracer concentration at a large time considered for a good mixing was ($C^{tmax}_{tracer} = 0.00135$). This means that the tracer concentration is invariable and the total tracer has been homogeneously distributed all around the tank. Then, additional stirring is not necessary.

7. Analysis of the Hydrodynamic Behavior

For understanding the hydrodynamic behavior inside the tank, an additional analysis was conducted for the best injection point (Pi_{18}). Figure 11a–c show the tracer concentration curves for different zones. The curves for the monitoring points near the impeller shaft are displayed in Figure 11a. The strongest influence of the impeller is on the monitoring point (Pm_{12}). This point is placed very near the injection point; then, it is quickly saturated in ex-

cess, showing the highest concentration values. As a consequence, these regions are quickly saturated; thus, only this curve will always remain over the final tracer concentration. Hence, this zone can be considered as a stagnant but also oversaturated region. In other words, a high tracer concentration remains around this zone without being distributed. After this, the tracer concentration is lightly reduced due to a slow distribution. The tracer concentration behavior is a sinusoidal damped curve, and the alternation is evidence of the strong influence provided by the impeller near the injection and monitoring points. This influence is reduced significantly on the point (Pm_7) with an intermediate position on the cylindrical tank. This curve remains without tracers and always is under the final tracer concentration until the homogeneity is reached. But, in the points far away from the impeller such as the monitoring points (Pm_1) and (Pm_2), this influence is very weak. The tracer concentration remains equal to zero, during the initial 25 s; the tracer is slowly dispersed and delays on arriving toward these zones. This behavior can be attributed to the joining between the shaft and the flat liquid surface. Finally, all the curves in Figure 11a are sinusoidal, and the homogenization is reached after 350 s, indicating a good mixing.
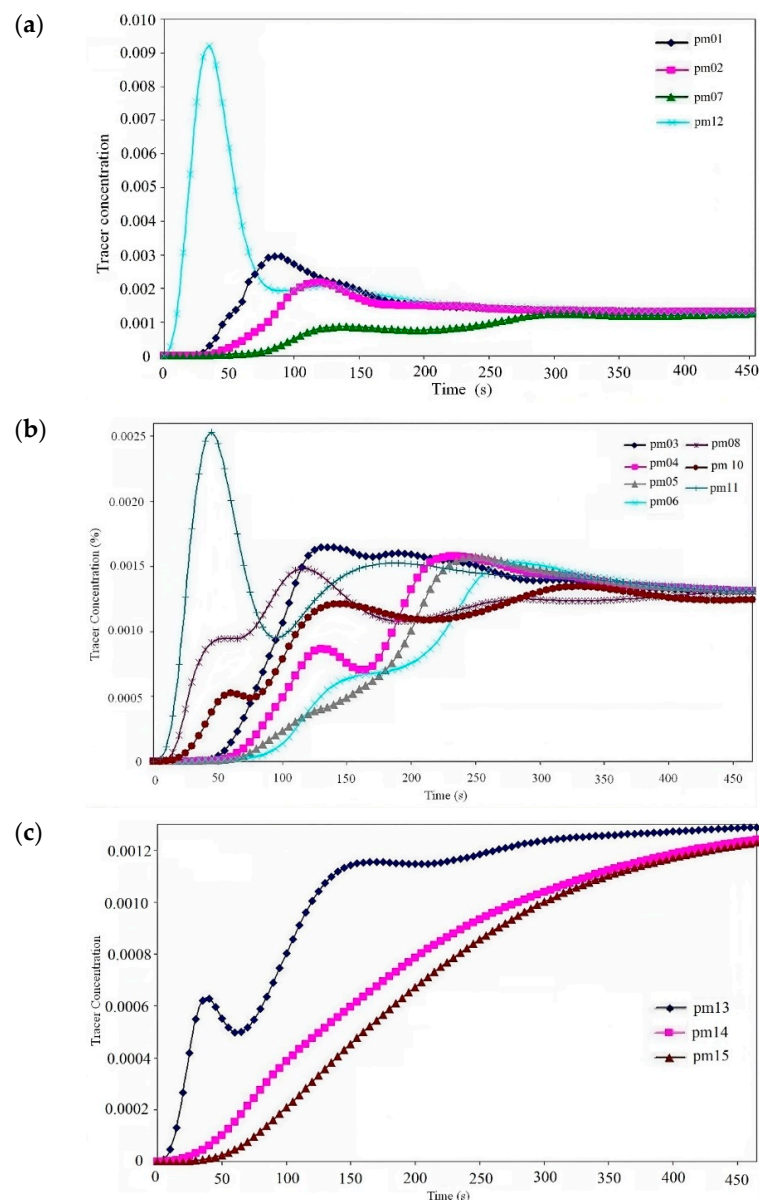

Figure 11. Tracer concentration curves on different regions inside the tank for monitoring points: (**a**) near the body impeller, (**b**) near the tank walls, and (**c**) in the bottom of the tank.

The monitoring points near the tank walls are shown in Figure 11b. The monitoring point Pm_{11} shows a similar behavior than the point Pm_{12}. The tracer concentration is quickly increased. Although the tracer concentration value is considerably more minor than in point (Pm_{12}), the sinusoidal behavior is also similar. Nevertheless, this point reaches the final tracer concentration value faster than the point Pm_{12} due to its fluctuations being lower. The points in the middle of tank body such as the Pm_8, Pm_9 and Pm_{10} also show a sinusoidal behavior, but these points remain briefly with a tracer concentration equal to zero; then, they begin to increase its tracer concentration. These curves always remain below the final tracer concentration value until reached. Curves for the points in the faraway positions such as Pm_3, Pm_4 and Pm_5 also remain below the final tracer concentration during the first 120 s and are damped curves due to the slow mixing process. Finally, the tracer concentration in the lowest region of the semispherical reactor has longer times without change ($C_{tracer} = 0$), as is shown in Figure 11c. The curves for the monitoring points Pm_{14} and Pm_{15} are parabolic due to the tracer being slowly dispersed here. Nevertheless, the curve for the point Pm_{13} is sinusoidal due to this point being the nearest to the impeller. These three curves also remain always below the final tracer concentration value: evidence again that the bottom is the most complicated region for distribution.

8. Validation of Hydrodynamics

Instability in tracer distribution curves is at the beginning of the time simulation due to the tracer being placed at a specific point and beginning to be distributed as the fluid forces impulses to move. Instability (tracer concentration variation) is the criterion to minimize the time required to obtain a homogeneous tracer distribution all around the tank. All simulations for every different injection point tend to be a common value. Then, the goal is to obtain the final tracer concentration in the shortest time.

Numerical methods and computer simulations have become a powerful tool to solve old complex problems. Increasing data store and management makes it possible to obtain accurate results quickly. Then, in this research, discretization of the lead volume on the tank was completed using different meshes. Information about these meshes used for discretization of the tank, impeller and lead volume is in Table 3. The tank and impeller are 3D bodies which were discretized using 2D meshes over their surfaces and then incorporated to the simulation. The lead volume inside was subtracted from the tank, and the impeller was defined and meshed using triangular, squared and hexagonal 2D elements which form tetragonal, hexagonal and honeycomb 3D meshes. The lead volume represented by every 3D cell is a tetragonal cell 9.676×10^{-7} m^3, hexahedral cell 9.6594×10^{-7} m^3, and honeycomb cell 9.71766×10^{-7} m^3, respectively; these are similar volumes which were selected to measure the efficacy of meshes.

Table 3. Features of meshes used for discretization.

	Area (m^2)	Volume (m^3)	Cells 2D Triangular	Cells 3D Tetragonal	Cells 3D Hexahedron	Cells 3D Honey Comb
Tank						
Cylindrical	0.66922	0.0716019649				
Semispherical	0.28445	0.0250888176				
total	0.951465	0.0966907825	1062			
shaft	0.147618		16,890			
impeller	0.00129032		657			
Lead volume (m^3)						
Cylindrical		0.0716019649	210,235	99,923		
Semispherical		0.0250888176				
total		0.0966907825		99,923	100,100	99,500

A comparison of results using hexahedron and honeycomb meshes is shown in Figures 12–16, taking the previously mentioned injection points ($P_{i=21}$, $P_{i=18}$, and $P_{i=11}$). Here, all the solutions tend to the final tracer concentration; then, it is possible to affirm the model works and results are reliable. Nevertheless, at the beginning of the simulation, there are notorious differences regarding approaching and variations. Simulations for the injection point $P_{i=21}$ is with a parabolic form due to the final tracer being slowly distributed from points near the top. Consequently, it takes longer for the tracer delay to be distributed. In contrast, simulations for the points $P_{i=18}$ and $P_{i=11}$ are with a sinusoidal form due to there being a dynamic tracer interchange as a result of the impeller movement, but the tracer is quickly distributed. Then, it is also possible to say all meshes tend to final tracer concentration, but the tetragonal mesh has reduced fluctuations. Additionally, the transitory states are the most complicated to calculate.
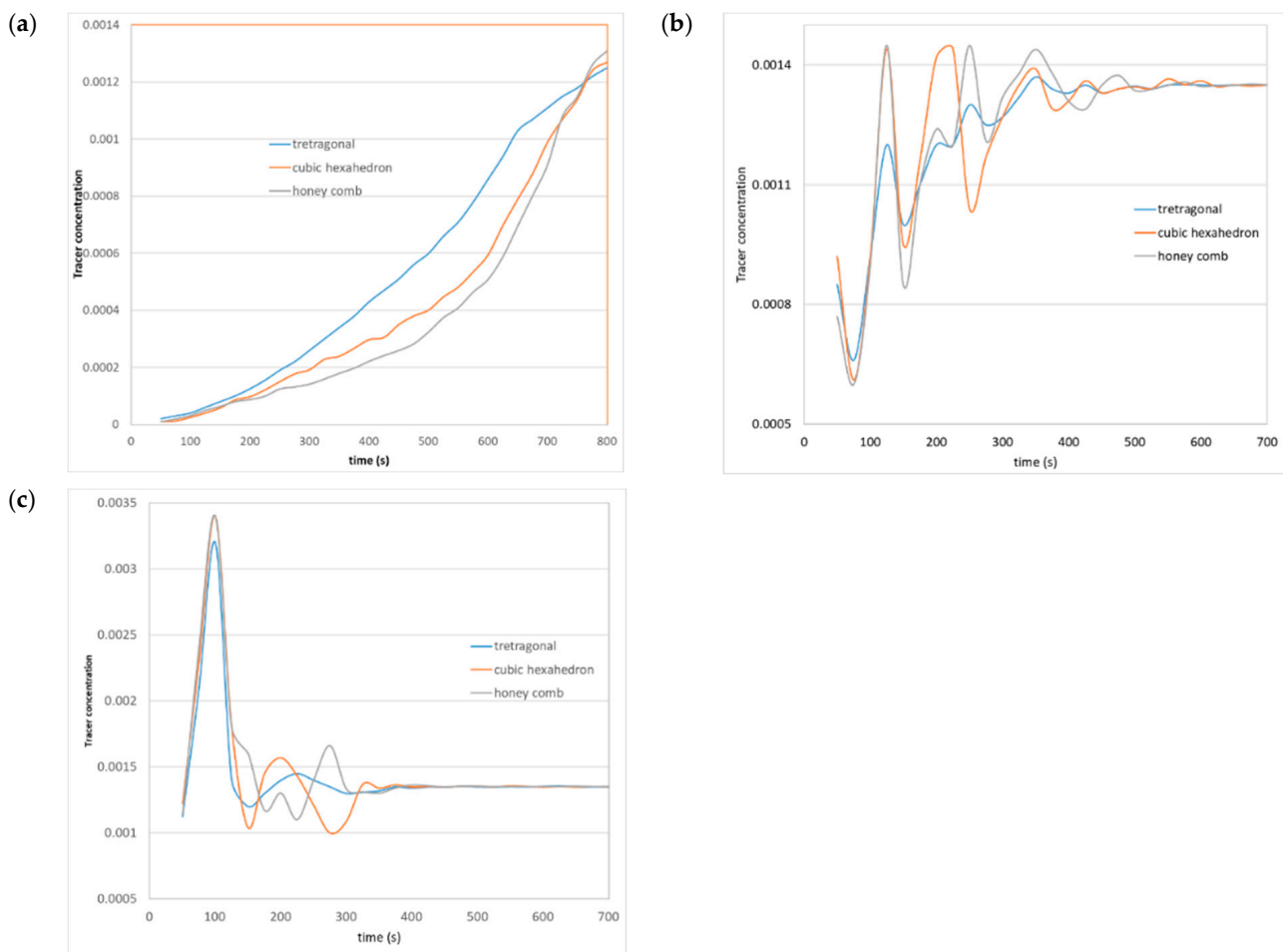

Figure 12. Comparison between different kinds of meshes used for simulation of the mixing process for (**a**) injection point ($P_{i=21}$), (**b**) injection point ($P_{i=18}$), the best injection point, (**c**) injection point ($P_{i=11}$).

Additionally, for comparison, the tracer concentration resulted for the injection points $P_{i=1}$, and $P_{i=9}$ on every monitoring point is shown in Figure 13a,b. Here, again, all curves tend to the final tracer concentration value, evidencing that this value can be considered as a feasible criterion for a homogeneous distribution. Some points near the impeller tend to the final tracer concentration, but other delays are longer. Then, the difference on tracer concentration is a measure of the hydrodynamic difficulty to distribute the tracer on every tank zone. Here, again, it is possible to appreciate that the tracer concentration variations are minor on all monitoring points for the injection point $P_{i=9}$. It is possible to appreciate

that monitoring points near the impeller tends to the final tracer concentration quickly, and that monitoring points placed near the injection points are with a notorious tracer excess. In contrast, monitoring points on the semispherical zone have a tracer deficit.
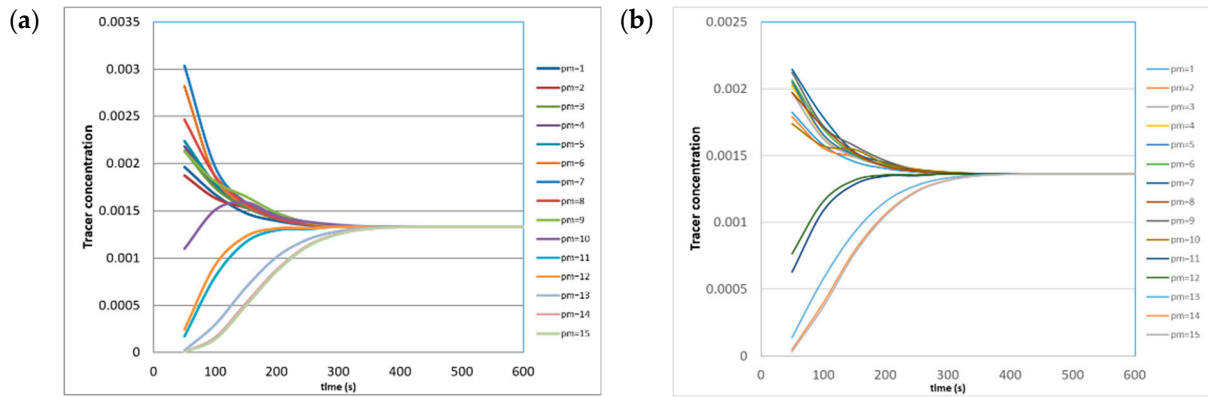

Figure 13. Tracer concentration on every monitoring point (**a**) for injection point $p_{i=1}$ and (**b**) for injection point $p_{i=9}$.
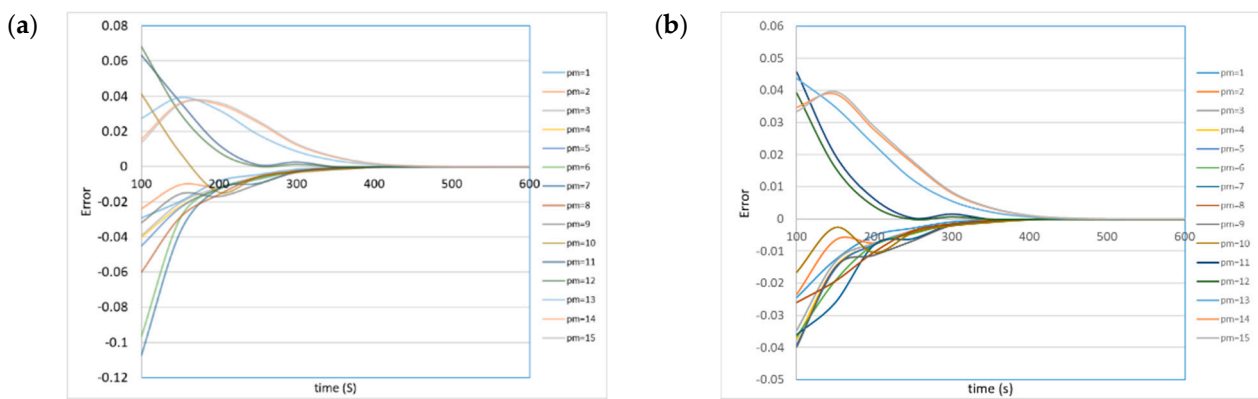

Figure 14. Error as a function of the tracer concentration on every monitoring point (**a**) for injection point $P_{i=1}$ and (**b**) for injection point $P_{i=9}$.
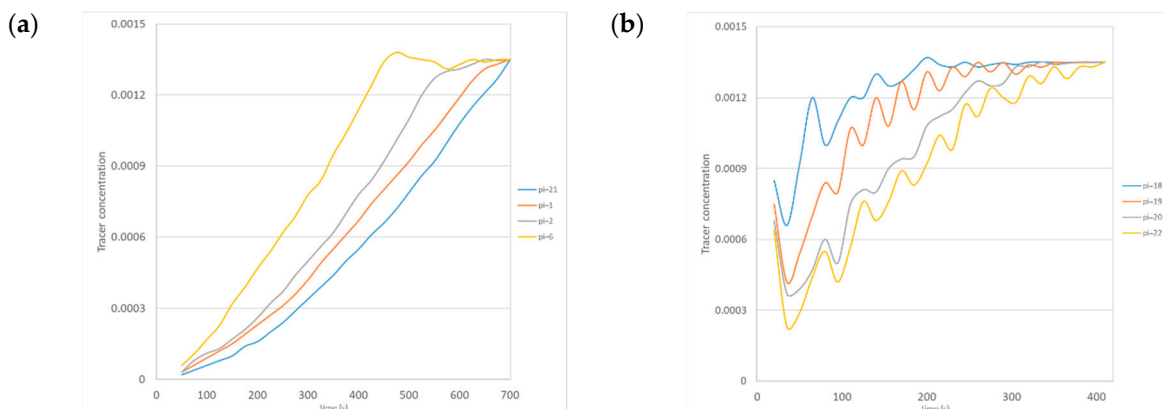

Figure 15. Tracer concentration on (**a**) the semispherical zone and (**b**) near the impeller influence.
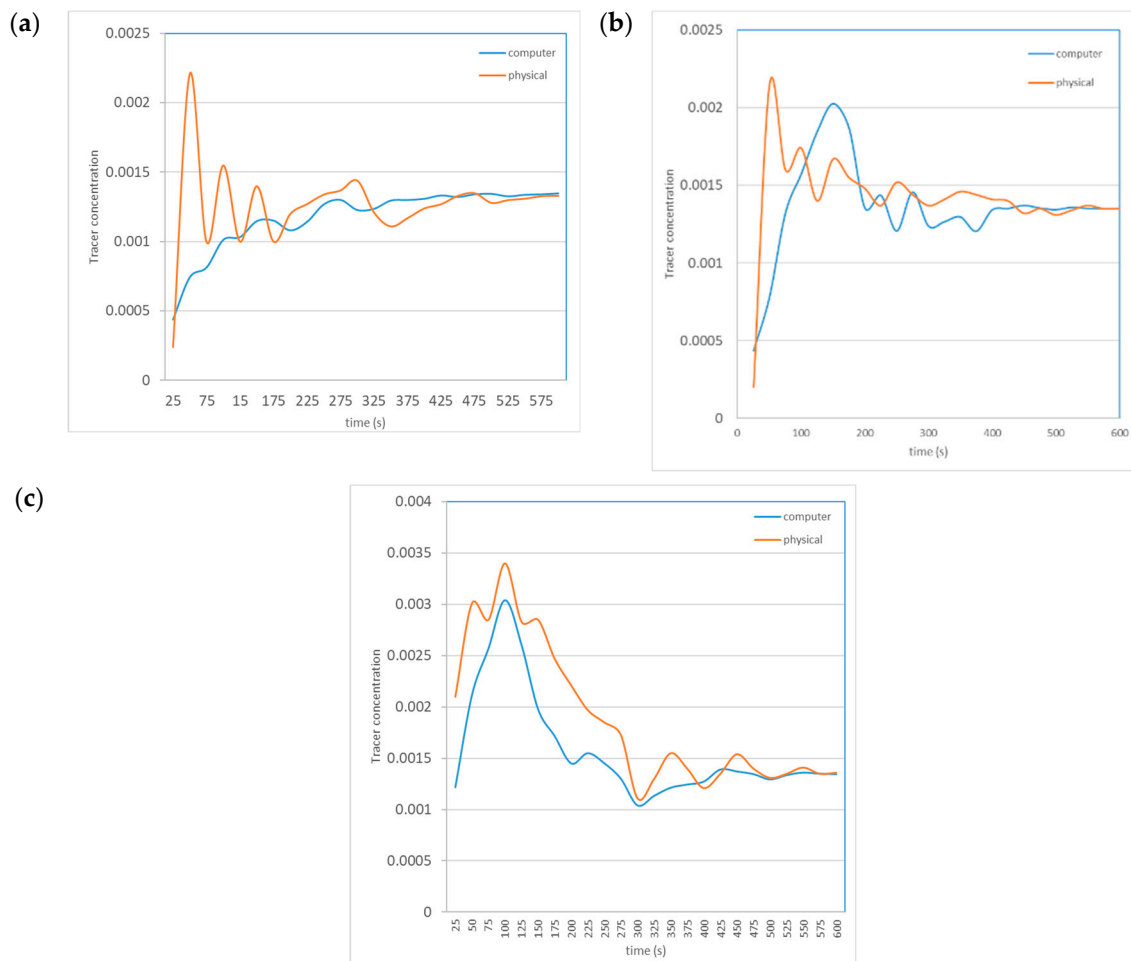
(a)

(b)

(c)

Figure 16. Comparison of results between computer simulation and physical modeling (**a**) for the injection point $P_{i=21}$, (**b**)for the injection point $P_{i=18}$, and (**c**) for the injection point $P_{i=11}$.

To know the homogeneity of the tracer distribution, Equation (13) was used to calculate variations respecting the last calculated values; then, the curves for every monitoring point tend to zero when the tracer has been homogeneously distributed, as shown in Figure 14a,b.

$$\text{Error} = 100 \, (C_{\text{tracer}}{}^{\Delta t} - C_{\text{tracer}}{}^{\Delta t - 1}) \tag{13}$$

Injection points $P_{i=21}$, $P_{i=1}$, $P_{i=2}$ and $P_{i=6}$ are with similar behaviors and are the most complicated for distribution; these points are near the upper wall and top of the tank. The tracer placed in these points initially is very far from the impeller influence. Velocity vectors are weak, and the inertial forces of the fluid move the tracer so slowly. An additional handicap against tracer distribution is the fact that properties of the tracer and melting lead are the same ($\rho_{\text{tracer}} = \rho_{\text{lead}}$); consequently, the influence of the buoyancy forces makes difficult to drive the tracer to the bottom of the tank. Industrially, this can be a serious problem if the density of the reacts added for the cleaning lead is equal to or less than lead density ($\rho_{\text{tracer}} < \rho_{\text{lead}}$). Then, the industrial suggestion was to place the reacts near the bottom tank. Moreover, the vector in the semispherical bottom impulses up the fluid. In the same way, the injection points $P_{i=18}$, $P_{i=19}$, $P_{i=20}$ and $P_{i=22}$ form a common area; these are the best injection areas due to the influence of the impeller being near. Then, the place tracer can be strongly impulsive, while tracer concentration on the semispherical zone and near the impeller influence denotes a very different hydrodynamic behavior, as can be seen in Figure 15a,b.

Finally, a comparison with a physical model is shown in Figure 16a–c. Here, it is evident for short times, there is a notorious difference between the computational mode using tetrahedral mesh and a model that was built. The physical model was built with a transparent acrylic: the scale was 1:11, the fluid used for representing lead was water, and the tracer was sodium chloride. A particle indicator velocimeter was used to measure the quantity of tracers passing across every monitoring point position. In these figures, there is also a tendency to the final tracer concentration calculated computationally, although variations can be appreciated during the transitory period due to the natural turbulence of the physical modeling.

Consequently, after the hydrodynamic analysis, the following criterion for identifying an improvement on the mixing process can be confirmed.

1. Curves of tracer concentrations tend to approach the final tracer concentration faster; thus, mixing time is reduced.
2. Fluctuation of the tracer concentration curve is minor.
3. Tracer in excess is minor, and it is quickly distributed.

Instability at the beginning of simulation is high, and the major variations between the physical model and computer simulations are at this instant of the simulation.

Inject reacts for cleaning in different points of the tank is the easiest way for modifying the industrial practices; then, this work represents the most economic form for improving. Suggestions for future works are to simulate the system including different properties for the tracer ($\rho_{\text{tracer}} \neq \rho_{\text{lead}}$) and modify the tracer volume at the initial condition to know if there is enough for the cleaning process or if the tracer volume can contribute to reduce the mixing time. Another option to explore is to simulate different tank configurations and different impeller configurations.

In addition, a comparison of simulations using different fine tetragonal meshes is shown in Table 4. Here, values of the stirring times required to obtain the final tracer concentration using the injection points $P_{i=21}$, $P_{i=18}$ and $P_{i=11}$ are employed to test the mesh influence. Fine mesh is expressed as a percentage of nodes listed in Table 4. Thus, a 200% mesh has double the nodes for discretization. Here, it is evident that the times vary with wider meshes, but its influence is reduced as the mesh became smaller.

Table 4. Times required for the final tracer concentration as a function of the fine mesh employed on the points $P_{i=21}$, $P_{i=18}$ and $P_{i=11}$.

Fine Mesh (%)	Time (s) for the Final Tracer Concentration		
	Pi_{18}	Pi_{11}	Pi_{21}
60	480	680	1015
80	475	635	945
Original	450	600	900
150	445	590	888
200	447	595	895
250	448	591	898
300	450	597	901

9. Influence of the Impeller Speed

Additional information can be obtained analyzing the influence of the impeller rotatory speed, as shown in Figure 17a–c. All these curves represent the global behavior for every impeller speed. All the curves are sinusoidal, but smoothing is different; some of them have excess and others have a deficit of tracer concentration; the lowest excess of the tracer appears in Figure 17a. These curves have a minor variation between them; moreover, all curves tend to the final tracer concentration quickly. Curves below the mixing time are slowly reduced as the impeller RPMs are increased. In Figure 17b, all curves are with an

excess of tracer at the beginning; these remain over the final tracer concentration for more than 150 s. Then, all of them are damped. The influence of the RPMs increment is minimal due to the analyzed point having an intermediate behavior. The highest tracer excesses are shown in Figure 17c; here, many curves remain with an excess of tracer remaining for at least 200 s, until these are damped. Nevertheless, the sinusoidal forms remain for 500 s. The increment on the impeller rotatory speed reduces the mixing time, but the influence of selecting an appropriated injection point is stronger.
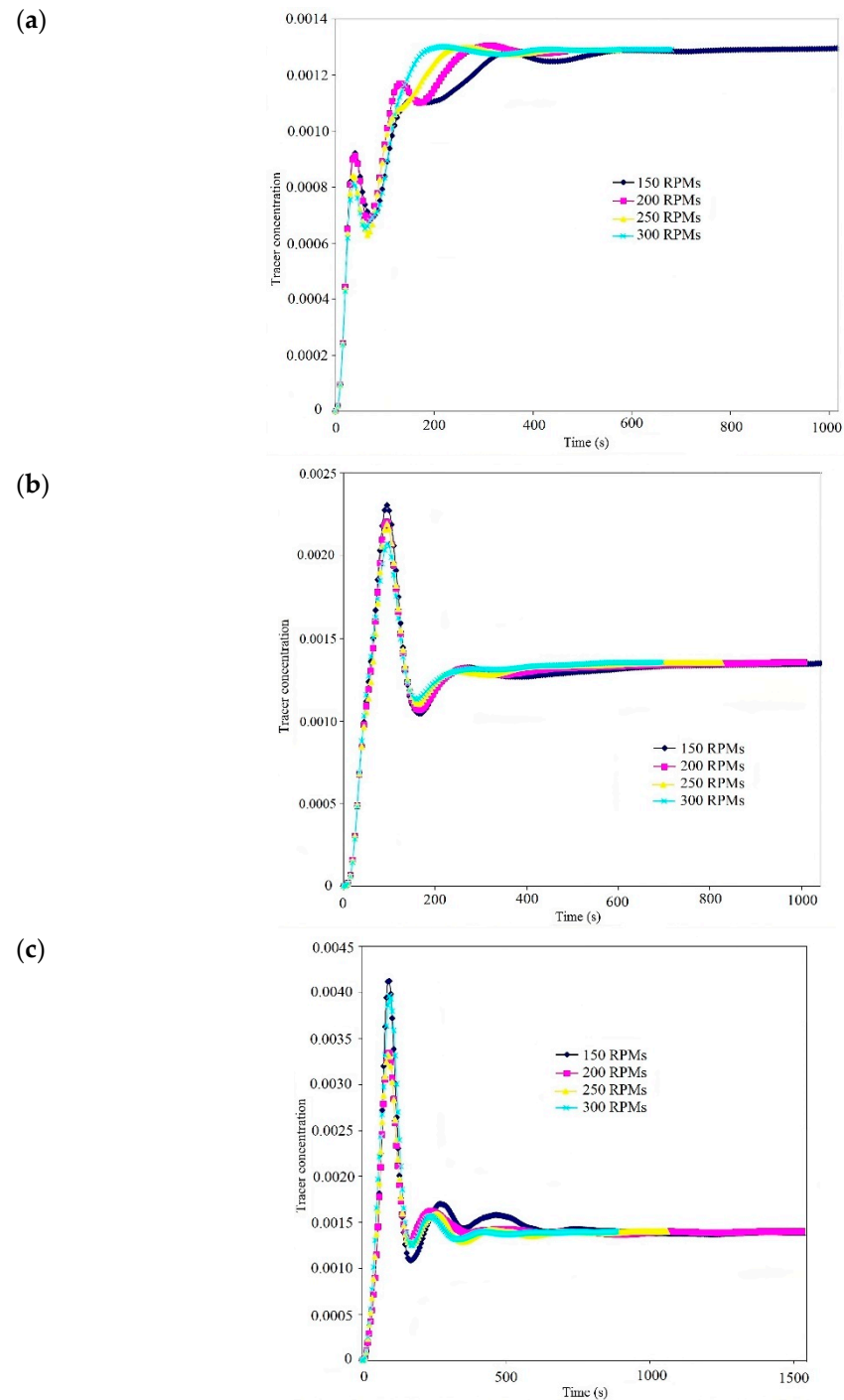

Figure 17. Tracer concentration curves for different impeller rotate speed corresponding to (**a**) the best injection point (P_{i18}), (**b**) an intermediate injection point (P_{i11}), and (**c**) the worst injection point (P_{i21}).

10. Conclusions

After analyzing of the cases simulated, the following conclusions can be drawn.

The tracer concentration in the monitoring points near the impeller is strongly influenced by the rotational speed and strong fluctuations of the tracer concentration can be observed; nevertheless, the tracer excess quickly is distributed due to the stirring.

Sinusoidal curves for tracer concentration are evidence of the instability of the system; the tracer here must be distributed to improve mixing; until all these curves are damped, the tracer concentration will tend to be homogeneous.

There are curves with sinusoidal and parabolic behavior; parabolic curves were frequently found in the bottom of the tank or near the surface of the tank due to these points being far away from the impeller influence. Consequently, parabolic curves always have a deficit of tracer concentration, and its presence indicates a poor mixing zone.

According to the simulations, it is unnecessary to run longer times due to the tracer having been homogeneously distributed, and the variation of concentration values is not significant. Consequently, employing extra times for mixing is also unnecessary.

The evolution of tracer concentration is a feasible parameter to evaluate mixing; it is evidence of a homogeneous distribution. Moreover, understanding the hydrodynamic dynamics inside the stirred lead reactor is very important to improve its performance.

The selection of the best injection point is very important to reduce unnecessary working times and improve industrial efficiency.

According to the simulations, it is possible to affirm that the tracer must be injected near the impeller in order to profit from the stirring forces. Therefore, the injection of a tracer on points near the top surface or reactor walls must be avoided due to these having the most delayed mixing times.

The semispherical region at the tank bottom is the most complicated region in which to distribute the tracer due to buoyancy forces, which force up the liquid. This reactor can be redesigned; a flat bottom configuration improves mixing.

References

1. Zhang, W.; Yang, J.; Wu, X.; Hu, Y.; Yu, W.; Wang, J.; Dong, J.; Li, M.; Liang, S.; Hu, J.; et al. A critical review on secondary lead recycling technology and its prospect. *Renew. Sustain. Energy Rev.* **2016**, *61*, 108–122. [CrossRef]
2. Li, Y.; Yang, S.; Taskinen, P.; He, J.; Liao, F.; Zhu, R.; Chen, Y.; Tang, C.; Wang, Y.; Jokilaakso, A. Novel recycling process for lead-acid battery paste without SO_2 generation—Reaction mechanism and industrial pilot campaign. *J. Clean. Prod.* **2019**, *217*, 162–171. [CrossRef]
3. Sun, Z.; Cao, H.; Zhang, X.; Lin, X.; Zheng, W.; Cao, G.; Sun, Y.; Zhang, Y. Spent lead-acid battery recycling in China—A review and sustainable analyses on mass flow of lead. *Waste Manag.* **2017**, *64*, 190–201. [CrossRef] [PubMed]
4. Prengaman, R.D.; Mirza, A.H. Recycling concepts for lead–acid batteries. In *Lead-Acid Batteries for Future Automobiles*; Elsevier: Amsterdam, The Netherlands, 2017; pp. 575–598. [CrossRef]
5. Moseley, P.T.; Rand, D.A.J.; Garche, J. Lead–acid batteries for future automobiles: Status and prospects. In *Lead-Acid Batteries for Future Automobiles*; Elsevier: Amsterdam, The Netherlands, 2017; pp. 601–618. [CrossRef]
6. Tian, X.; Gong, Y.; Wu, Y.; Agyeiwaa, A.; Zuo, T. Management of used lead acid battery in China: Secondary lead industry progress, policies and problems. *Resour. Conserv. Recycl.* **2014**, *93*, 75–84. [CrossRef]
7. Sloop, S.E.; Kotaich, K.; Ellis, T.W.; Clarke, R. RECYCLING | Lead–Acid Batteries: Electrochemical. In *Reference Module in Chemistry, Molecular Sciences and Chemical Engineering*; Ames Laboratory (AMES): Ames, IA, USA, 2021.
8. Garche, J.; Dyer, C.K.; Moseley, P.T.; Ogumi, Z.; Rand, D.A.; Scrosati, B. (Eds.) *Encyclopedia of Electrochemical Power Sources*; Elsevier: Amsterdam, The Netherlands, 2009; pp. 179–187.

9. Choi, B.S.; Wan, B.; Philyaw, S.; Dhanasekharan, K.; Ring, T.A. Ring, Residence Time Distributions in a Stirred Tank: Comparison of CFD Predictions with Experiment. *Ind. Eng. Chem. Res.* **2004**, *43*, 6548–6556. [CrossRef]
10. Guha, D.; Ramachandran, P.; Dudukovic, M. Flow field of suspended solids in a stirred tank reactor by Lagrangian tracking. *Chem. Eng. Sci.* **2007**, *62*, 6143–6154. [CrossRef]
11. Wang, F.; Mao, Z.-S.; Wang, Y.; Yang, C. Measurement of phase holdups in liquid–liquid–solid three-phase stirred tanks and CFD simulation. *Chem. Eng. Sci.* **2006**, *61*, 7535–7550. [CrossRef]
12. Hartmann, H.; Derksen, J.J.; van den Akker, H.E.A. Numerical simulation of a dissolution process in a stirred tank reactor. *Chem. Eng. Sci.* **2006**, *61*, 3025–3032. [CrossRef]
13. Hildebrandt, T.; Osada, A.; Peng, S.; Moyer, T.J. Standards and tests for lead–acid batteries in automotive applications. In *Lead-Acid Batteries for Future Automobiles*; Elsevier: Amsterdam, The Netherlands, 2017; pp. 551–573. [CrossRef]
14. Blanpain, B.; Arnout, S.; Chintinne, M.; Swinbourne, D.R. Chapter 8—Lead Recycling. In *Handbook of Recycling: State-of-the-Art for Practitioners, Analysts, and Scientists*; Elsevier: Amsterdam, The Netherlands, 2014; pp. 95–111. [CrossRef]
15. Bailey, C.; Kumar, S.; Patel, M.; Piper, A.W.; Fosdick, R.A.; Hance, S. Comparison between CFD and measured data for the mixing of lead bullion. In Proceedings of the Second International Conference on CFD in Minerals and Process Industries CSIRO, Melbourne, Australia, 6–8 December 1999; pp. 351–356.
16. Huang, S.; Mohamad, A.; Nandakumar, K. Numerical Analysis of a Two-Phase Flow and Mixing Process in a Stirred Tank. *Int. J. Chem. React. Eng.* **2008**, *6*, A38. [CrossRef]
17. Koh, P.T.L.; Xantidis, F. CFD Modelling in the scale-up of a stirred reactor for resin beads. In Proceedings of the Second International Conference on CFD in Minerals and Process Industries CSIRO, Melbourne, Australia, 6–8 December 1999; pp. 369–374.
18. Murthy, B.N.; Deshmukh, N.A.; Patwardhan, A.W.; Joshi, J.B. Hollow self-inducing impellers: Flow visualization and CFD simulation. *Chem. Eng. Sci.* **2007**, *62*, 3839–3848. [CrossRef]
19. Zhang, Z.; Chen, G. Liquid mixing enhancement by chaotic perturbations in stirred tanks. *Chaos Solitons Fractals* **2008**, *36*, 144–149. [CrossRef]
20. Rahimi, M.; Parvareh, A. CFD study on mixing by coupled jet-impeller mixers in a large crude oil storage tank. *Comput. Chem. Eng.* **2007**, *31*, 737–744. [CrossRef]
21. Sossa-Echeverria, J.; Taghipour, F. Computational simulation of mixing flow of shear thinning non-Newtonian fluids with various impellers in a stirred tank. *Chem. Eng. Process. Process Intensif.* **2015**, *93*, 66–78. [CrossRef]
22. Lassin, A.; Piantone, P.; Burnol, A.; Bodénan, F.; Chateau, L.; Lerouge, C.; Crouzet, C.; Guyonnet, D.; Bailly, L. Reactivity of waste generated during lead recycling: An integrated study. *J. Hazard. Mater.* **2007**, *139*, 430–437. [CrossRef]
23. Weidenhamer, J.D.; Clement, M.L. Evidence of recycling of lead battery waste into highly leaded jewelry. *Chemosphere* **2007**, *69*, 1670–1672. [CrossRef] [PubMed]
24. Milewska, A.; Molga, E. CFD simulation of accidents in industrial batch stirred tank reactors. *Chem. Eng. Sci.* **2007**, *62*, 4920–4925. [CrossRef]
25. Karcz, J.; Cudak, M.; Szoplik, J. Stirring of a liquid in a stirred tank with an eccentrically located impeller. *Chem. Eng. Sci.* **2005**, *60*, 2369–2380. [CrossRef]
26. Szalai, E.; Arratia, P.; Johnson, K.; Muzzio, F. Mixing analysis in a tank stirred with Ekato Intermig® impellers. *Chem. Eng. Sci.* **2004**, *59*, 3793–3805. [CrossRef]
27. Pinho, F.T.; Piqueiro, F.M.; Proença, M.F.; Santos, A.M. Turbulent flow in stirred vessels agitated by a single, low-clearance hyperboloid impeller. *Chem. Eng. Sci.* **2000**, *55*, 3287–3303. [CrossRef]
28. Vite-Martinez, P.; Ramírez-López, A.; Romero-Serrano, A.; Chávez-Alcalá, F.; López-Ramírez, S. Improving of Mixing Efficiency in a Stirred Reactor for Lead Recycling Using Computer Simulation. *Inz. Miner.* **2014**, *16*, 25–32.
29. Vite-Martínez, P.; Durán-Valencia, C.; Cruz-Maya, J.; Ramírez-López, A.; López-Ramírez, S. Optimization of reagents injection in a stirred batch reactor by numerical simulation. *Comput. Chem. Eng.* **2014**, *60*, 307–314. [CrossRef]
30. Zhang, Y.; Chen, C.; Lin, W.; Yu, Y.; E, D.; Wang, S. Numerical Simulation of Tracers Transport Process in Water Model of a Vacuum Refining Unit: Single Snorkel Refining Furnace. *Steel Res. Int.* **2020**, *91*, 2000022. [CrossRef]
31. Wang, S.; Li, Z.; He, C.; Liu, D.; Zou, G. An Integrated Method for Modular Design Based on Auto-Generated Multi-Attribute DSM and Improved Genetic Algorithm. *Symmetry* **2021**, *14*, 48. [CrossRef]
32. Theyab, S.D.; Atshan, W.G.; Lupaş, A.A.; Abdullah, H.K. New Results on Higher-Order Differential Subordination and Superordination for Univalent Analytic Functions Using a New Operator. *Symmetry* **2022**, *14*, 1576. [CrossRef]
33. Li, L.-C.; Xu, B. CFD simulation of floating particles suspension in a stirred tank. *Chem. Pap.* **2017**, *71*, 1377–1387. [CrossRef]
34. Pan, H.; Geng, Y.; Dong, H.; Ali, M.; Xiao, S. Sustainability evaluation of secondary lead production from spent lead acid batteries recycling. *Resour. Conserv. Recycl.* **2019**, *140*, 13–22. [CrossRef]
35. Escudié, R.; Liné, A. Analysis of turbulence anisotropy in a mixing tank. *Chem. Eng. Sci.* **2006**, *61*, 2771–2779. [CrossRef]
36. Colli, A.N.; Bisang, J.M. Evaluation of the hydrodynamic behavior of turbulence promoters in parallel plate electrochemical reactors by means of the dispersion model. *Electrochim. Acta* **2011**, *56*, 7312–7318. [CrossRef]
37. Zhao, H.-L.; Zhang, Z.-M.; Zhang, T.-A.; Liu, Y.; Gu, S.-Q.; Zhang, C. Experimental and CFD studies of solid–liquid slurry tank stirred with an improved Intermig impeller. *Trans. Nonferrous Met. Soc. China* **2014**, *24*, 2650–2659. [CrossRef]
38. Gong, Y.; Tian, X.-M.; Wu, Y.-F.; Tan, Z.; Lv, L. Recent development of recycling lead from scrap CRTs: A technological review. *Waste Manag.* **2016**, *57*, 176–186. [CrossRef]

39. Tamburini, A.; Cipollina, A.; Micale, G.; Brucato, A.; Ciofalo, M. Influence of drag and turbulence modelling on CFD predictions of solid liquid suspensions in stirred vessels. *Chem. Eng. Res. Des.* **2014**, *92*, 1045–1063. [CrossRef]

40. Morales, R.D.; Calderon-Hurtado, F.A.; Chattopadhyay, K. Demystifying Underlying Fluid Mechanics of Gas Stirred Ladle Systems with Top Slag Layer Using Physical Modeling and Mathematical Modeling. *ISIJ Int.* **2019**, *59*, 1224–1233. [CrossRef]

41. Ramírez-López, A.; Muñoz-Negrón, D.; Palomar-Pardavé, M.; Romero-Romo, M.A.; Gonzalez-Trejo, J. Heat removal analysis on steel billets and slabs produced by continuous casting using numerical simulation. *Int. J. Adv. Manuf. Technol.* **2017**, *93*, 1545–1565. [CrossRef]

42. Ouyang, X.; Lin, W.; Luo, Y.; Zhang, Y.; Fan, J.; Chen, C.; Cheng, G. Effect of Salt Tracer Dosages on the Mixing Process in the Water Model of a Single Snorkel Refining Furnace. *Metals* **2022**, *12*, 1948. [CrossRef]

43. Wadnerkar, D.; Tade, M.O.; Pareek, V.K.; Utikar, R.P. CFD simulation of solid–liquid stirred tanks for low to dense solid loading systems. *Particuology* **2016**, *29*, 16–33. [CrossRef]

44. Wadnerkar, D.; Utikar, R.P.; Tade, M.O.; Pareek, V.K. CFD simulation of solid–liquid stirred tanks. *Adv. Powder Technol.* **2012**, *23*, 445–453. [CrossRef]

45. Xie, L.; Luo, Z.-H. Modeling and simulation of the influences of particle-particle interactions on dense solid–liquid suspensions in stirred vessels. *Chem. Eng. Sci.* **2018**, *176*, 439–453. [CrossRef]

46. Gu, D.; Liu, Z.; Xie, Z.; Li, J.; Tao, C.; Wang, Y. Numerical simulation of solid-liquid suspension in a stirred tank with a dual punched rigid-flexible impeller. *Adv. Powder Technol.* **2017**, *28*, 2723–2734. [CrossRef]

47. Tamburini, A.; Cipollina, A.; Micale, G.; Brucato, A.; Ciofalo, M. CFD simulations of dense solid–liquid suspensions in baffled stirred tanks: Prediction of solid particle distribution. *Chem. Eng. J.* **2013**, *223*, 875–890. [CrossRef]

48. Tamburini, A.; Cipollina, A.; Micale, G.; Brucato, A.; Ciofalo, M. CFD simulations of dense solid–liquid suspensions in baffled stirred tanks: Prediction of the minimum impeller speed for complete suspension. *Chem. Eng. J.* **2012**, *193–194*, 234–255. [CrossRef]

49. Bai, H.; Stephenson, A.; Jimenez, J.; Jewell, D.; Gillis, P. Modeling flow and residence time distribution in an industrial-scale reactor with a plunging jet inlet and optional agitation. *Chem. Eng. Res. Des.* **2008**, *86*, 12. [CrossRef]

50. Zughbi, H.D.; Ahmad, I. Mixing in Liquid Jet-Agitated Tanks: Effects of Jet Asymmetry. *Ind. Eng. Chem. Res.* **2005**, *44*, 1052–1066. [CrossRef]

51. Xu, Z.; Yang, C.; Zhang, Z.; Liu, B.; Jin, Z. Study on the Numerical Model of Dense Solid Suspension Driven by a Coaxial Mixer. *Ind. Eng. Chem. Res.* **2021**, *60*, 1939–1951. [CrossRef]

52. Zhou, Y.; Wang, L.; He, H.; Sun, J. Mixing Process in a Tank Stirred with Improved Double Intermig Impellers. *J. Chem. Eng. Jpn.* **2019**, *52*, 719–729. [CrossRef]